PHYSICAL REVIEW MATERIALS **3**, 093604 (2019)

Surface and dislocation investigation of planar GaN formed by crystal reformation of nanowire arrays

Jovana Colvin,[1] Rafal Ciechonski,[2] Filip Lenrick,[3] Olof Hultin,[4] Maryam Khalilian,[5] Anders Mikkelsen,[1]
Anders Gustafsson,[5] Lars Samuelson,[5] Rainer Timm,[1] and B. Jonas Ohlsson[6]
[1]*Synchrotron Radiation Research and NanoLund, Lund University, Box 118, 221 00, Lund, Sweden*
[2]*Glo AB, Ideon Science Park, Scheelevägen 22, S-223 63 Lund, Sweden*
[3]*Centre for Analysis and Synthesis and NanoLund, Lund University, Box 124, 221 00 Lund, Sweden*
[4]*RISE Research Institutes of Sweden, Scheelevägen 17, S-223 70, Lund, Sweden*
[5]*Solid State Physics and NanoLund, Lund University, Box 118, 221 00 Lund, Sweden*
[6]*Hexagem AB, Ideon Science Park, Scheelevägen 15, S-223 70 Lund, Sweden*

(Received 19 July 2019; published 25 September 2019)

In this paper we present a process of forming monolithic GaN surface from an ordered nanowire array by means of material redistribution. This process, referred to as reformation, is performed in a conventional MOVPE crystal growth system with the gallium supply turned off and allows a crystal nanostructure to change shape according to differences in surface energies between its facets. Using reformation, coalescence may proceed closer to thermodynamic equilibrium, which is required for fabrication of high-quality substrate material. Scanning probe techniques are utilized, complemented by cathodoluminescence and electron microscopy, to investigate structural and electrical properties of the surface after reformation, as well as to assess densities, location, and formation of different types of defects in the GaN film. Spatial variations in material properties such as intrinsic majority-carrier types can be attributed to the radical changes in growth conditions required for sequential transition between nanowire growth, selective shell growth, and reformation. These properties enable us to assess the impact of the process on densities, locations, and formation of different types of dislocations in the GaN film. We find a fraction of the nanowires to comprise of a single electrically neutral edge dislocation, propagating from the GaN buffer, while electrically active dislocations are found at coalesced interfaces between nanowires. By decreasing the mask aperture size and changing the nucleation conditions the prevalence of nanowires comprising edge dislocation was significantly reduced from 6% to 3%, while the density of interface dislocations was reduced from 6×10^8 to 4×10^7 cm^{-2}. Using a sequential reformation process was found to create inversion domains with low surface potential N-polar regions in an otherwise Ga-polar GaN film. The inversion domains were associated with pinned dislocation pairs, and were further confirmed by selective wet etching in NaOH. This lateral polarity inversion was thoroughly eliminated in samples formed by a continuous reformation process. These results reveal a path and challenges for growing GaN substrates of superior crystal quality through nanowire reformation.

DOI: 10.1103/PhysRevMaterials.3.093604

I. INTRODUCTION

Radio frequency (RF) and power electronics both stand at tipping points where silicon technology is running out of steam. Requirements on speed, energy efficiency, and voltage tolerance can make the change to a better adapted semiconductor material inevitable. Gallium nitride (GaN) provides excellent properties for RF, opto, and power electronics, having a wide, direct band gap as well as high thermal stability. Despite progress in device technology and performance [1], GaN technology is limited by the crystal quality achieved in large scale semiconductor wafers. For other semiconductors of technological importance, high quality commercial substrates are almost exclusively grown from melt, most often by the Czochralski liquid phase epitaxy technique. Unfortunately, this method is not viable for GaN, which requires extreme conditions, with the best estimate known to date being 6 GPa and 2600 K to form a congruent melt [2]. Alternative bulk growth methods, which do not utilize a GaN melt, can only produce small and expensive GaN substrates. Instead, synthesis of commercial GaN substrates mainly relies on heteroepitaxy on sapphire, silicon, or silicon carbide. The lattice size and thermal expansion coefficient of these crystals are different from GaN, creating a material mismatch which is the main source of extended defect networks, mainly threading dislocations (TDs), in heteroepitaxial GaN substrates. High densities of TDs limit device performance by Coulomb scattering, increased nonradiative recombination, and vertical leakage paths [3–7] resulting in reduced device breakdown voltage [8], the latter providing a particular challenge to the development of GaN vertical device architectures.

To date, wide-ranging avenues for improving GaN crystal quality have been investigated. Most efforts and results rely on epitaxial lateral overgrowth (ELO), capable of achieving reduced densities of TDs by filtering through patterned substrates [9–13]. The ELO technology utilizes (1) selective area growth from mask openings [14,15], and (2) growth anisotropy due to varying growth rates of different crystal facets [16]. The technology can be implemented in metalorganic vapor phase epitaxy (MOVPE), which is the primary technique used for GaN device growth. Selectively grown pyramids [15] and nanocolumns [17,18] have also been used as templates for subsequent ELO. Although noticeable improvement was made, appreciable amounts of defects were generated where nonaligned growth fronts emerge. Thus ELO remains a laboratory method; its cost and complexity are also impediments to commercial use.

Here we perform a detailed investigation of continuous GaN films formed from regularly spaced hexagonal nanowire (NW) arrays. Our fabrication method comprises coalescence of GaN from NW-based three-dimensional (3D) structures through a crystal reformation step. The method has two main advantages over previous approaches: efficient dislocation filtering, inherent to the NW growth step, and a coalescence step which can be performed appreciably closer to thermodynamic equilibrium than conventional MOVPE growth. The investigated samples are based on a hexagonal array of GaN core-shell NWs, selectively grown on a GaN/sapphire substrate using a nanopatterned mask. After the NW growth, the sample is annealed in an ammonia (NH_3)-rich atmosphere, in order for the 3D structures to spontaneously reform and coalesce into a single, monolithic planar GaN layer. This reformation step is driven by differences in the 3D-structure facet surface energies, in contrast to conventional MOVPE where supersaturation is mainly driven by elevated gas-phase concentrations of source material. This step has also been successfully implemented in fabrication of InGaN LEDs [19].

The initial NW growth and the reformation process are the critical steps of our approach. Therefore, we here investigate the surface morphology and electrical and optical properties of coalesced GaN films from a set of samples that allows a distinct comparison of epitaxial approach of these two steps and their impact on material quality of the reformed planar layer. Atomic force microscopy (AFM) and its derivatives, including conductive AFM (c-AFM), Kelvin probe microscopy (KPM), and scanning capacitance microscopy, are utilized. Along with the AFM techniques, we use transmission electron microscopy (TEM), scanning electron microscopy (SEM), and cathodoluminescence spectroscopy. These techniques are implemented in order to correlate electrical, optical, and structural properties with the epitaxial structure and the prevalence of defects.

Inhomogeneities in cathodoluminescence data have previously been attributed to local defect distributions [20]. Hansen *et al.* [21] showed the possibilities of scanning capacitance microscopy by studying the charge state of defects in GaN films, while Koley *et al.* [22] estimated the density of surface states based on the measured values of Schottky barrier heights extracted from Kelvin probe data. Furthermore, a combination of KPM and c-AFM has been used to investigate electrical properties such as charge state and conductivity for different types of dislocation [23]. We go a step further and implement all the above mentioned techniques to map the growth-structure structurally (SEM), topographically (AFM), carrier type (SCM), and optically by CL. AFM is also used to identify and count dislocations, and, where possible, also determine their type. The origin of dislocations is determined by TEM. CL and SCM are used to reveal dislocations along the coalesced interface. We use c-AFM to identify and count electrically active dislocations and inversion domain boundaries. The extension of the inversion domains is revealed by KPM. Based on this in-depth characterization, we explore specific types of TDs, their locations and origins.

We distinguish edge, screw, and mixed type dislocations at the interfaces of coalesced NWs, in addition to edge dislocations in some of the NW cores. We show paths, related to specific growth conditions, on how to reduce densities of these dislocations. Furthermore, we identify N-polar inversion domains by correlating Kelvin probe, conductive AFM and TEM results, with selective etching of N-polar GaN in NaOH solution [24–29]. These inversion domains are associated with significant current leakage at the domain boundaries and pinned dislocations. Their formation is found to be caused by a sequential reformation process, and they can be avoided by using a continuous step reformation approach instead.

II. EXPERIMENTAL DETAILS

A. Nanowire growth and coalescence

The epitaxial growth process, which was performed in one sequence, can be divided into four steps: nucleation, NW growth, volume growth, and crystal reformation. Growth was performed in a Thomas Swan 3 × 2 in. close-coupled showerhead MOVPE reactor. All samples were grown on commercial *n*-type GaN buffer layers, grown on *c*-plane sapphire substrates. The dislocation density of the GaN buffer layer is 3×10^8 cm^{-2} as measured by XRD. This agrees well with the number of 5×10^8 cm^{-2} which we obtained by AFM. A 100 nm thick Si_3N_4 mask was placed on the substrate and patterned by nanoimprint lithography, resulting in a regular array of 160 nm wide circular openings for samples A and B (140 nm for sample C), with a pitch of 0.7 μm. These openings expose the underlying GaN crystal and act as nucleation sites for the NW growth without any deposits formed on the mask.

The NWs were grown using either trimethylgallium (TMG) or triethylgallium (TEG) and ammonia (NH_3) at a temperature of 930 °C with molecular V/III ratios of 8. Source flows of 1.95×10^{-3} standard l min^{-1} (TMG) and 3.5×10^{-3} standard l min^{-1} (NH_3) or 1.1×10^{-1} standard l min^{-1} (TEG) and 3.2×10^{-3} standard l min^{-1} (NH_3) were used. Surface-selective growth conditions manifested in hexagonal NWs with six $\{1\bar{1}00\}$ *m* planes, a flat (0001) *c* plane, and six small inclined $\{10\bar{1}1\}$ facets, as shown in Figs. 1(a)–1(c). The diameter of the NWs (short diagonal) is ~250 nm, and the *m* planes are ~730 nm in height.

For promoting uniform shell growth around the NW core, the V/III ratio was increased to approximately 7000:1, and the temperature was decreased to 880 °C. Growth of the $\{10\bar{1}1\}$ facets was comparatively slow, leading to a pyramidal NW shape, as can be seen in Figs. 1(d)–1(f). The shell growth was continued until the *m* planes of neighboring NWs were approximately 50 nm apart from each other in samples B and C while 100 nm apart in sample A, retaining approximately equal volume of deposited material between all three samples.

Coalescence of the GaN core-shell NW structures was achieved by reformation of the GaN material of the pyramids, leading to coalescence and planarization of the sample. For this step, the temperature was increased to 980 °C. In the

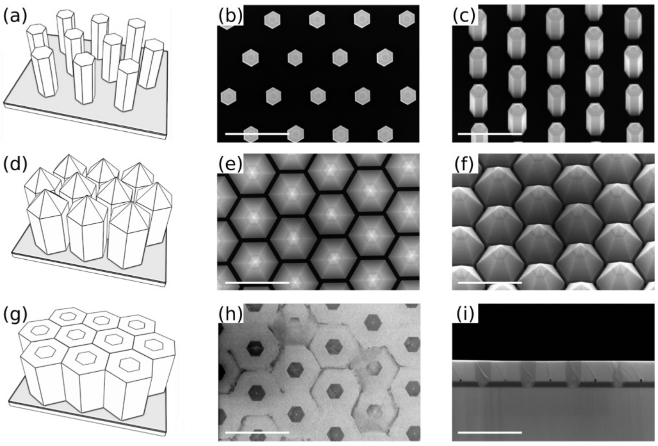

FIG. 1. Reformation process. Schematics of (a) NW cores, (d) NW shell growth, and (g) the sample after NW reformation, together with corresponding SEM images in top view (b), (e), and (h), under an angle of 30° (c) and (f), and in cross section (i). Scale bars are 1 μm in all images.

growth of samples B and C the flow of the Ga precursor was entirely shut off, while the NH_3 flow was kept at 2 standard l min^{-1}. The reformation process for sample A was different, using a sequential loop of a short growth step (100 s, TEG-flow 0.18 standard l min^{-1} and NH_3 flow of 6.5 standard l min^{-1}), followed by a step with Ga source-flow shut off (733 s). This loop was repeated 10 times. Figures 1(g)–1(i) depicts a flat continuous film formed upon crystal reformation step (sample B). We observed a rather flat *c* plane formed during the coalescence, having no memory of the $\{10\bar{1}1\}$ facets. A contrast difference between NW core, shell, and coalesced material is apparent in the SEM top view image of Fig. 1(h). The cross-sectional SEM image [Fig. 1(i)] shows a continuous GaN film, approximately 500 nm thick, resulting from the reformation process. It can also be seen that the coalescence has left voids between the bottom parts of the NWs, terminated by the NW *m* planes, underneath the continuous film.

B. Characterization

SEM images were recorded in a Hitachi SU8010 cold field emission SEM setup with secondary electron detector. Electron beam energies of 10–15 kV were chosen, unless otherwise specified.

The cathodoluminescence study was done in a conventional SEM with a liquid-helium cold stage. Monochromatic images and hyperspectral maps were recorded at 10 K and room temperature, using a probe current of 50 pA and an acceleration voltage of 5 kV.

The surface morphology was studied by AFM with a Nanowizard II microscope from JPK Instruments and a Bruker dimension icon (300) microscope. The Nanowizard AFM was operated in amplitude modulated mode employing highly *n*-doped Si cantilevers (PPP-NCH from Nanosensors) with a nominal force constant of 42 N m^{-1} and resonance frequency of 330 kHz. The dimension icon AFM was operated in Peak Force Tapping$^{\text{TM}}$ mode, employing Sb *n*-doped Si cantilevers (Bruker RTESPA-300) with a nominal force constant of 40 N m^{-1} and resonance frequency of 300 kHz.

In both AFM instruments, a number of electrical AFM modes were used in order to correlate surface morphology and electrical properties. Local conductivity of the sample was evaluated in the Nanowizard instrument with a JPK conductive AFM module operating in constant force, static mode using overall PtSi-coated cantilevers (PtSi-CONT from Nanosensors) with a nominal force constant of 0.2 N m^{-1} and resonance frequency of 13 kHz. A low current (maximum ±100 nA) amplifier with a gain of 10^8 V A^{-1} and a noise limit of 0.5 pA RMS was utilized to measure the local current. In the Bruker dimension icon AFM, the PeakForce TUNA module was implemented, which provides higher sensitivity and is capable of detecting currents down to the sub-pA range. Although operated in dynamic mode, all figures show contact current, that is, the average current measured while the cantilever was in the repulsive regime during its force-distance cycle. During this period, a nanoscopic Schottky contact was formed between the PtSi-coated tip and the sample. For both current-evaluating techniques, the current was measured while a sample bias of 10 V was applied to the sample and the AFM probe kept at ground potential, that is, under reverse bias condition. While reverse bias inhibit current flow by increasing the width of the Schottky-induced depletion region, it also reveals positions where leakage occurs. In this way c-AFM gives information about the exact position of leakage paths, which may be caused by conductive dislocations or tunneling through defect-related states.

Open loop scanning capacitance microscopy (SCM) imaging was performed in contact mode to map the two-dimensional distribution of electrical charge carriers inside the GaN films. For this, we utilized a Bruker SCM application module with a sensitivity of down to 10^{-22} FHz$^{-1/2}$. PtIr-coated cantilevers (Bruker SCM-PIT) with a nominal spring constant of 2.8 N m^{-1} and resonance frequency of 50 kHz were used. The metal (tip)–insulator (GaN native oxide)–semiconductor (GaN sample) junction acts as a capacitor, where a high frequency AC bias voltage was applied to the sample while the probe tip measured the induced dC/dV capacitance variation. The amplitude of the AC bias of (4 V) and an additional small DC (−0.5 V) bias applied to the sample were chosen such that the sample under the tip alternated between accumulation and depletion of charge carriers. dC/dV phase and amplitude channels are shown in this work, along with the corresponding topography data. The phase is sensitive to the type of the charge carriers (*p*- or *n*-type carriers or intrinsic material), and the amplitude to the charge carrier density: A material with a lower charge carrier density depletes faster, resulting in a larger dC/dV slope and a higher amplitude signal, and vice versa.

The local surface potential of the GaN film was mapped in the Nanowizard AFM using a JPK Kelvin probe microscopy (KPM) module in the amplitude modulation mode, using the same cantilevers as for standard morphology imaging. KPM was operated in lift mode, meaning that the surface topography was acquired in forward scanning direction, and the surface potential in reverse scanning direction while the probe tip was kept around 50 nm above the surface and repeating the height trajectory of the forward scan. A silicon sample

TABLE I. Outline of experimental differences in growth conditions between samples A, B, and C.

Sample	Aperture size	Growth	Reformation
A	160 nm	TMG (HT nucleation)	Sequential (10×)
B	160 nm	TMG (HT nucleation)	Continuous
C	140 nm	TEG (LT nucleation)	Continuous

with aluminum and gold patterns was used for calibrating the Kelvin potential difference between sample and tip, allowing mapping of relative differences in surface potential with a correct contrast scale.

TEM and scanning TEM (STEM) images were recorded at 300 kV in a JEOL 3000F microscope with an annular dark-field detector and a $2k \times 2k$ CCD camera. For TEM analysis, a small lamella was cut out of the sample by focused ion beam (FIB), using a FEI Nova NanoLab 600 dual beam FIB/SEM equipped with an Omniprobe micromanipulator. The lamella was capped with platinum, and polished down to a thickness of 100 nm.

Chemical etching of coalesced GaN samples was carried out using a 2 molar sodium hydroxide (NaOH) unagitated solution heated to 70 °C. The samples were etched for 30 min in darkness.

III. RESULTS AND DISCUSSION

Three samples (A, B, and C) have been investigated, representing different NW growth and nucleation conditions and different reformation procedures, as described in Table I. Representative AFM images of the three samples are shown in Fig. 2. The reformation step, which is the final step in the epitaxial sequence, generally produces smooth *c*-plane surfaces by material redistribution. In the following, we will first present structural, electrical, and optical properties of the reformed surface after reformation related to the different growth conditions. In the second part, we will discuss three types of dislocations observed in our samples, their origins, and how they can be reduced in density or completely avoided by choosing appropriate growth conditions.

A. Surface properties after reformation

The surface of sample A, grown by a sequential reformation process, is characterized by an intricate step pattern, as shown in Fig. 2(a), with atomically flat terraces extending over several hundred nm. They are interrupted by single or double GaN (0001) steps (half or full values of the lattice constant $c \approx 0.52$ nm). Sample A also exhibits hexagonal voids of varying sizes at locations between NWs, indicating incomplete coalescence and/or dislocations. Samples B and C are fully coalesced after a continuous reformation step. Hexagonal hillocklike features, with varying height and shape, are prevalent in sample B, see Fig. 2(b), while we also observe the NW pattern, smooth surface curvatures, and single or double step-high steps in samples B and C [Figs. 2(b) and 2(c)].

The root-mean-square (RMS) roughness of samples A, B, and C over the areas indicated in Fig. 2 amounts to 16, 33, and 6 nm, respectively. It should be noted that these surfaces are obtained directly by the reformation process, and that their roughness can be reduced significantly by overgrowth. Indeed, growing a 2 μm thick GaN layer on top of sample A resulted in an RMS value of only 0.4 nm, comparable with the original substrate.

Having evaluated the general morphology, we review its correlation to local electrical and optical properties that are common to all three samples. They are summarized for different characterization techniques in Fig. 3, obtained for sample B.

Scanning capacitance microscopy emphasizes the distribution of free charge carriers in the reformed GaN film. Figures 3(a)–3(c) are obtained simultaneously, showing (a) height information, (b) the dC/dV phase, corresponding to carrier type, and (c) the dC/dV amplitude, corresponding—at least qualitatively—to the carrier concentration. The measurements reveal variations in charge concentration at the reformed GaN surface, corresponding to a mosaic surface of hexagonal patterns comprising NW cores and NW shells, joined by the reformed, coalesced material, which already was visible in Fig. 1(h). The phase channel (b) shows the NW cores and the coalesced matrix material to be *n* type, whereas the NW shells are *p* type. Nonintentionally doped GaN (0001) surfaces have been reported to show *n*-type conductivity due to silicon [30] and oxygen [31] impurities, while a *p*-type

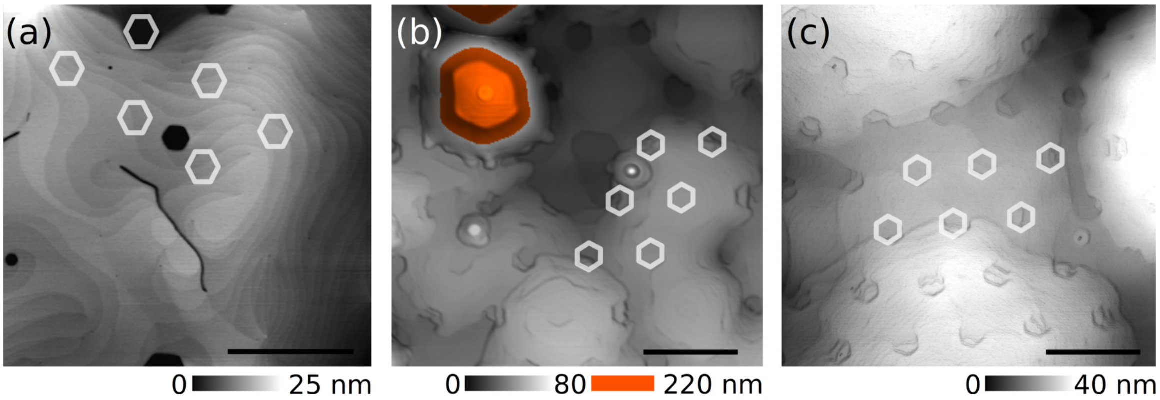

FIG. 2. AFM topography images of samples A (a), B (b), and C (c). Flat terraces and surface steps of mainly single or double GaN(0001) step height can be observed. The scale bars correspond to 1 μm. Color scale reflects the range of the z region being displayed. Positions of the hexagonal NW cores are indicated in some parts of the images by white hexagons.

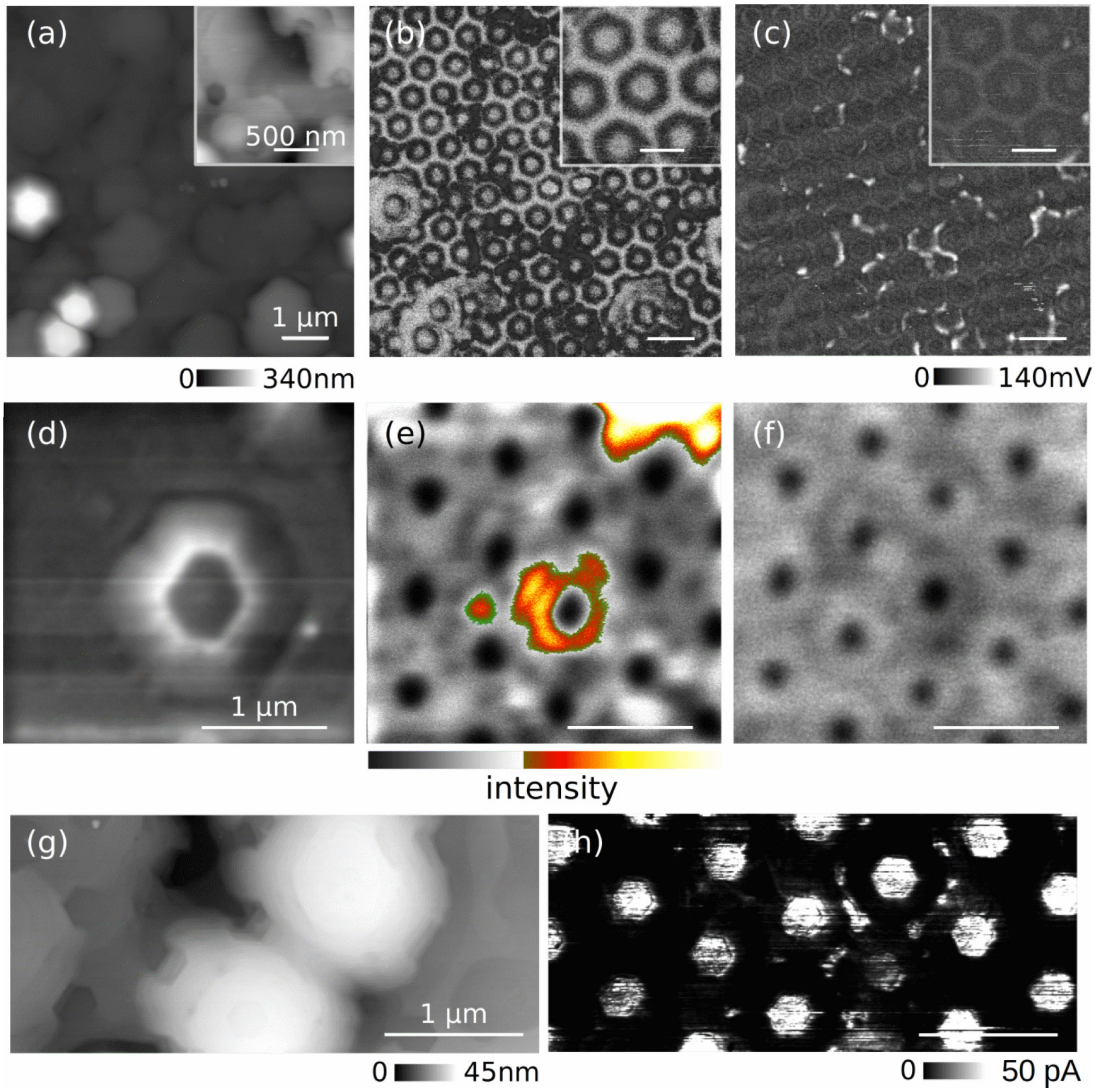

FIG. 3. Optical and electrical properties. (a)–(c) Simultaneously acquired AFM images showing (a) topography, (b) phase, and (c) amplitude of scanning capacitance microscopy dC/dV signal. Unintentionally n-doped NW cores and coalesced material (bright) and unintentionally p-doped shells (dark) can be distinguished in (b). Brighter contrast in (c) corresponds to regions with lower charge carrier density and vice versa. Insets in (a)–(c) show higher resolution and higher contrast images of a representative area. (d) SEM image together with (e) and (f) monochromatic CL images of the same region at emission energies of (e) 3.46 eV, corresponding to the near band edge signal, and (f) 3.27 eV, attributed to Mg impurities. (g) and (h) AFM images showing (g) topography and (h) current map.

behavior is uncommon for unintentionally doped GaN. In the dC/dV amplitude signal displayed in Fig. 3(c), a higher signal (brighter contrast) corresponds to lower charge carrier concentrations and vice versa. The core/shell/coalesced-material matrix generally shows a rather homogeneous charge carrier concentration, with an in average ~10% lower signal (higher concentration) at the shells.

A monochromatic cathodoluminescence image is shown in Fig. 3(e), with a detection energy of 3.46 eV, corresponding to near band edge emission. GaN band edge emission is observed both from the NW shells and the coalesced material, with some spatial variations throughout the coalesced matrix. Notably stronger emission is found around a number of cores which comprise a rather tall and steep hillock on top. These structural features, seen in the SEM image of Fig. 3(d), have typical heights of 200–300 nm, and they are Ga rich according to energy-dispersive TEM data. The higher luminescence intensity is attributed to the larger volume of reformed material. In Fig. 3(f) the cathodoluminescence emission at an energy of 3.27 eV is attributed to Mg which can be explained by a memory effect in the epitaxial reactor [32], mainly released during the high-temperature reformation step. It appears to be uniformly distributed over the sample, except for the NW cores and corresponding hillocks, with less fluctuations than in the band gap emission. At higher magnification, we identify that the Mg-related emission is stronger from the shell than from the coalesced material, agreeing with the p-type surface character of the shell seen by capacitance measurements.

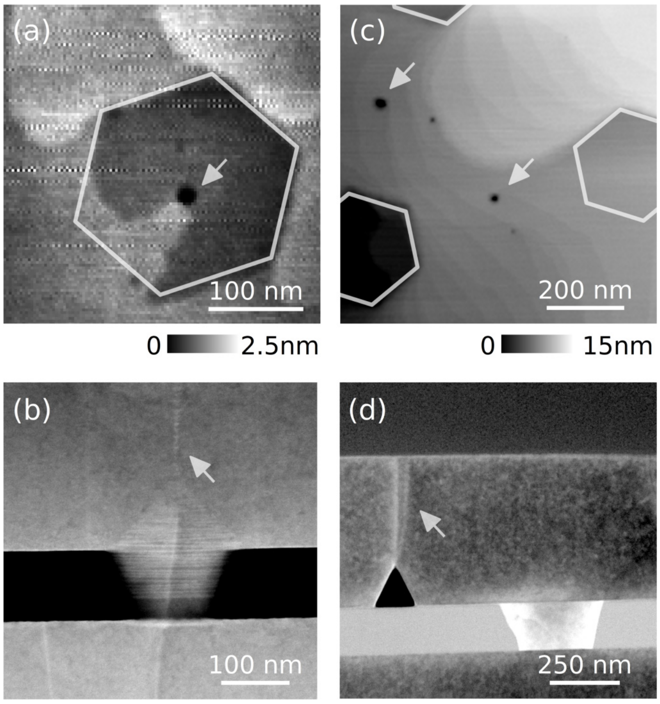

FIG. 4. Dislocations. (a) and (c) AFM images highlighting dislocations (indicated by arrows) at (a) in the center of a NW core and in (c) at the coalesced interface. The positions of some NW cores are indicated by hexagons. (b) and (d) Cross-sectional low-angle annular dark field STEM images showing paths of threading dislocations propagating from the growth substrate through a NW core (b), and at the interface (d). The SiN growth mask appears black in (b) and bright in (d). Voids resulting from the reformation process can be seen as dark triangles in (d).

Hardly any signal is observed from the NW cores, though they do emit in the yellow band (not shown here).

The local surface current map is obtained by conductive AFM. Figures 3(g) and 3(h) show the AFM topography and the current map recorded with a conductive AFM probe under 10 V sample bias. In this current image, we observe a leakage current over *n*-type NW cores with current levels of 200 pA, while no current is observed at the NW shells and most of the coalesced region.

B. Extended defects

The primary aim of this work is to investigate the formation and distribution of different types of defects in the reformed GaN layer. Individual defects were visible, though not highlighted, in Figs. 2 and 3. Their behavior and origin are examined in Figs. 4 and 5. The defects found have different origins, some propagating through the NW cores from the planar GaN buffer layers, others formed at the interface between coalesced neighboring NWs. The occurrence of these defects is different for samples A, B, and C. This can often be attributed to differences in the epitaxial growth of the samples in this study, as will be discussed in the following.

1. Dislocations propagating through the NW cores

Edge dislocations can be found in the middle of the NWs cores, as shown in the AFM image of Fig. 4(a). These are the remains of threading dislocations (TDs) formed by heteroepitaxial growth of the GaN buffer on the sapphire substrate, inevitably formed due to lattice and thermal mismatch between the sapphire and GaN crystals [33,34]. The origin of these dislocations is visible in the TEM image of Fig. 4(b), showing a TD propagating through an aperture in the Si_3N_4 mask and continuing through the nanowire, terminating at the free *c*-plane surface, where it is visible to AFM as in Fig. 4(a). The AFM morphology reveals them as pits in the surface, often merging into terraces [see Fig. 4(a)] without step termination, which is known as a signature of pure edge dislocations.

From the AFM data we obtain that 6% of the nanowires in sample B contain edge dislocations, resulting to a dislocation density of 1.4×10^7 cm^{-2}, while the density amounts to 6.6×10^6 cm^{-2} in sample C, corresponding to 3% of the NWs. The TD density of the GaN buffer layer grown on the sapphire substrate is evaluated as approximately 5×10^8 cm^{-2}, from AFM characterization of reference samples. The up to two orders of magnitude reduced defect density of the coalesced film indicates that most dislocations from the GaN buffer are filtered by the Si_3N_4 mask or bent away from the surface upon NW nucleation and growth. We note that sample C has a slightly smaller mask aperture size than sample B, approximately 140 vs 160 nm, but also that the NW-core growth conditions are different between the two samples. We therefore conclude that the 23% smaller aperture area, the lower temperature during NW nucleation, the different precursor during initial NW growth (TEG instead of TMG), or a combination of these three parameters, has led to improved dislocation filtering resulting in the 2 times lower density of the defects per nanowire of sample C compared to sample B.

2. Dislocations originating from the coalesced interface

A second origin of dislocations is found in the *m*-plane interfaces where NWs coalesce during the reformation, shown in Figs. 4(c) and 4(d). Such dislocations can be found at one, several, or all six *m*-plane interfaces around a NW. They may form networks that comprise interfaces between multiple NWs. Appreciable areas without interface dislocations are also observed. TEM images [see Fig. 4(d)] confirm that they are indeed situated at the joining position between two NWs, while AFM images [see Fig. 4(c)] show them either terminating a surface step, indicating a TD of screw or mixed character, or merging into a terrace, without step termination, indicating a TD of pure edge character.

The influence of these dislocations on material properties is seen in the cathodoluminescence image of Fig. 3(e), where the band edge emission is found to be reduced locally at the boundaries of the NWs, indicating nonradiative recombination at the position of the dislocations. This has been correlated to the presence of screw and mixed TDs which have been reported to be electrically active [35–37]. However, the mechanism for this leakage current is not yet fully understood, with some authors proposing incorporation of excess gallium [35] and others reporting oxygen related impurities in the vicinity of screw dislocation cores [36]. Indeed, our conductive AFM results show current levels of approximately 50 pA [see Fig. 3(h)] at the position of electrically active TDs.

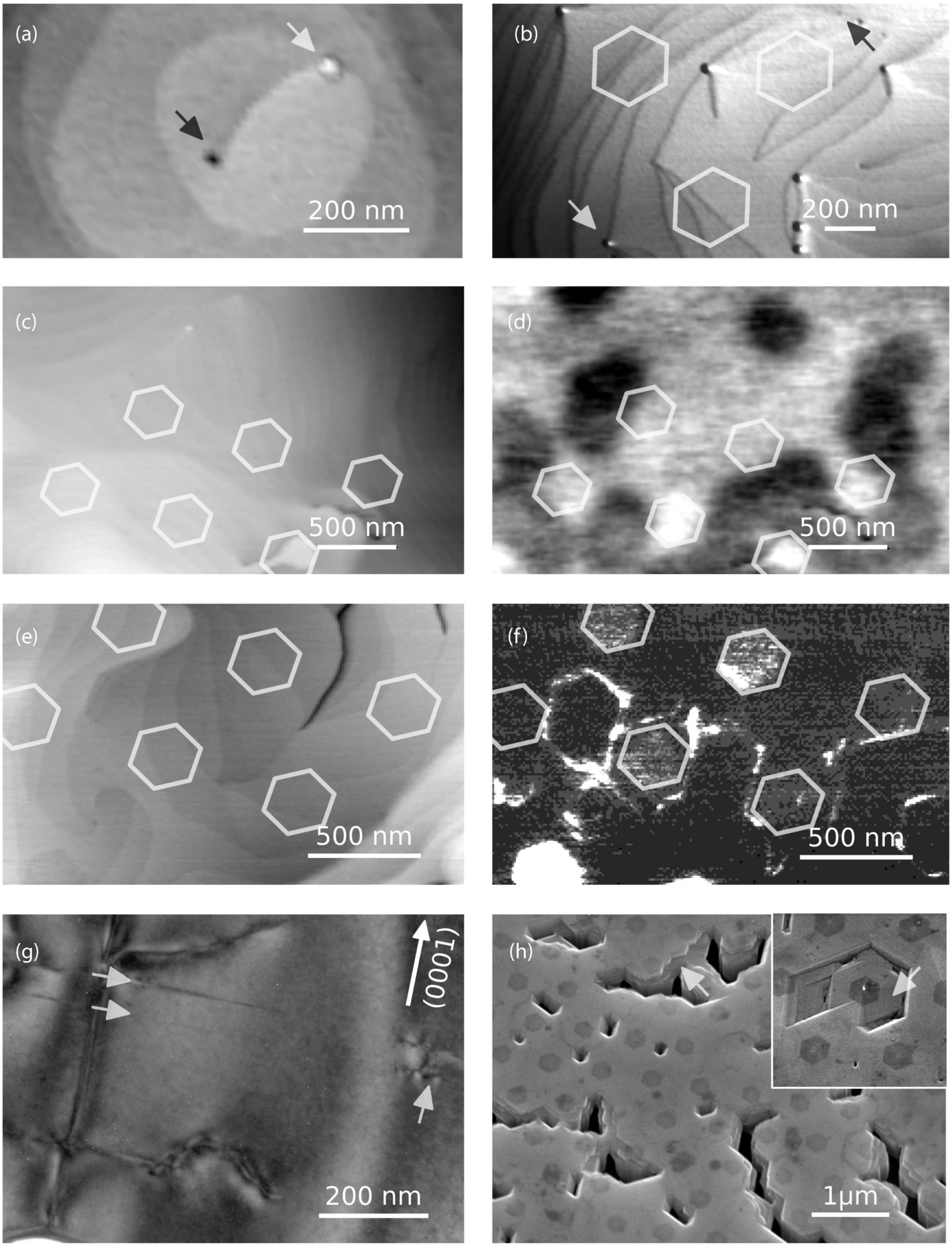

FIG. 5. Defects in sample A. (a) and (b) 3D AFM topography images of pinned dislocations, comprising of small protrusion (indicated by white arrows) and small pits (black arrows). (c) AFM topography image and (d) surface potential map obtained by Kelvin probe microscopy at the same position. Areas with 100–150 meV lower (dark) surface potential indicate inversion domains. (e) and (f) Simultaneously acquired (e) AFM topography and (f) current map. (g) Cross-sectional TEM image. Threading dislocations are penetrating along the (0001) direction. Short dark stripes perpendicular to the (0001) direction (highlighted by arrows) indicate lateral polarity inversion. (h) SEM image of the sample surface after etching in NaOH. Slanted facets (highlighted by arrows in inset) can be seen, again indicating lateral polarity inversion.

The density of these dislocations determined by conductive AFM is approximately 2×10^8, 6×10^8, and 4×10^7 cm^{-2} in samples A, B, and C, respectively. Scanning capacitance microscopy, as shown in Figs. 3(b) and 3(c), records a p-type carrier signal at the position of these dislocations, and a dC/dV amplitude signal which is appreciably higher than that of the surrounding coalesced matrix, shell, and NW core material, indicating an electrically active behavior.

Interface dislocations often form at adjacent interfaces, this can be seen in the scanning capacitance or conductive AFM images of Figs. 3(c) and 3(h). The formation of interface dislocations is most likely due to coalescence of slightly misaligned NW structures. The prevalence of these dislocations is not homogeneously distributed over the surface. Dislocation free regions are an indication that they can be minimized by further improving the reformation conditions. Most importantly, comparing samples C and B, which are grown with identical reformation parameters, a decrease of more than an order of magnitude in the density of interface dislocations is seen in sample C, indicating that nucleation and initial NW core growth also affect the formation and prevention of interface dislocations.

One configuration of interface dislocations was only found in sample A, Figs. 5(a) and 5(b). It comprises spatially separated pinned dislocations, connected by a (a) double or (b) single surface step as indicated by arrows. The steps terminate at the dislocations, often extending over the nanowire cores. Structural properties of these TD pairs are visualized in Fig. 5(a) where two dislocations are positioned at the common terrace with one forming a small hill and the other forms a small pit. We have also observed a configuration of pinned pit-pit [38] and pinned hill-hill dislocations. In addition, Kelvin probe microscopy [see Figs. 5(c) and 5(d)] reveals that the pits have a 50 ± 5 meV lower surface potential than the surrounding coalesced matrix, while no potential difference is observed for their protruding counterparts.

3. *Inversion domains*

Besides individual dislocations, the Kelvin probe images also reveal regions with a potential 100–150 meV lower than that of the surrounding surface, indicated dark in Fig. 5(d). These regions are typically confined to the area surrounding the NW cores and can span over several μm. This surface potential difference is in the range reported for Ga- versus N-polar GaN [39–41]. Although the exact potential shift will also depend on the sample preparation, doping concentration, surface treatment, surface band bending, as well as the AFM lift height, we tentatively associate these two-dimensional defects to regions with N-polar inversion domains, in the elsewhere Ga-polar crystal matrix.

Conductive AFM results of the same sample, acquired with a 10 V sample bias, are shown in Figs. 5(e) and 5(f). The observed current [Fig. 5(f)] cannot be correlated with the topography [Fig. 5(e)], as no height change is measured over paths with strongly varying conductance. Varying current levels are observed at the NW cores, which will be discussed separately in a different publication [42], but also along paths in the crystal matrix surrounding the NW cores. While the leakage paths do not correspond to the coalescence boundary between neighboring nanowires, nor the NW cores, they delineate borders, similar to patterns and sizes of the dark areas in the Kelvin probe images. We therefore interpret these paths as electrically conductive inversion domain boundaries, likely of Holt type [43].

The pinned dislocations and the inversion domains are only observed in sample A, which has been reformed through a 10× sequence of growth and anneal steps, in contrast to continuously reformed samples B and C. Additional samples reformed by sequential approach, including AlN/GaN structures also show the same type of inversion domains (not shown here). It is clear that the sequential reformation procedure imposes a vertical/lateral layer-by-layer formation process to the coalesced GaN material. This was investigated by TEM of sample A, see Fig. 5(g). Several defects along the basal plane can be seen in the reformed layer which is in agreement with lateral inversion domain boundaries (IDBs) [44]. They are seen to traverse through the coalesced interface dislocations. An example of two defects terminating at the coalesced interface is indicated by arrows. Polarity change by lateral growth on masked substrates is a subject of extensive study [45–47].

The existence of areas with N polarity in sample A was confirmed by NaOH etch. Figure 5(h) shows surface morphology obtained by SEM after 30 min of etching. We observe extended etch features attributed to the removal of N-polar GaN [29]. The surface of the etched sample A shows varying etching depths for the larger lateral inversion domains, indicating different height of the domains corresponding to the formation at different steps of the reformation sequence. Importantly, the etched areas again correspond in size, shape, and distribution to the regions with lower surface potential and electrically active borders [Figs. 5(d) and 5(f)]. The surface structure as obtained in Fig. 5(h) remains the same even after prolonged etching times, showing a self-limiting nature of the etching process once the inversion domains have been etched. Along with the removal of lateral N-polar domains, etch pits are present along the coalesced interface associated with pinned dislocations. Protruding dislocations are unstable against NaOH, while their pit pair counterpart remains unaffected. It should be noted that screw, edge, and mixed TDs are etch resistant in all our samples, and they cannot be correlated to etched regions.

Samples B and C were stable against polarity-selective NaOH etch. This is not surprising with regards to sample C, with significantly different nucleation and core growth conditions compared with samples A and B. However, sample B, with identical nucleation and core growth conditions as sample A, would be expected to etch in a similar fashion as sample A, if the inversion domains were correlated to NW growth. Instead, it is the somewhat foliated configuration of inversion domains with different etching depth, unique for sample A, that correlates their origin with the reformation process, recalling that coalescence here was achieved through a repeated sequence of anneal and growth steps. Importantly, changing the coalescence conditions to a continuous reformation process could eliminate the presence of polarity inversion and pinned dislocations.

IV. CONCLUSIONS

A method enabling formation of continuous planar GaN substrate layers has been devised. The critical planarization step is performed without supply of Ga source material, allowing reformation of crystal material from 3D NW-based structures into a continuous coalesced layer. Two potential advantages of this procedure over the current technology are the opportunity to form a planar GaN layer without the TDs that are prevalent in heteroepitaxial GaN buffers, by the use of the formation of the monolithic GaN planar layer at conditions appreciably closer to thermodynamic equilibrium than conventional MOVPE growth. Both these aspects provide increased freedom to minimize dislocation densities and improve material properties of GaN substrates, including leakage, breakdown voltage, electron mobility, and thermal conductivity, compared to traditional epitaxial fabrication methods on non-native substrates.

Functional samples with variations in growth conditions have been characterized, mainly by scanning probe methods. Nonconductive edge type dislocations were observed in the center of some NWs, indicating that the used apertures still are too large for efficient dislocation elimination. However, the density of core dislocations could already be reduced by 50% through reducing the aperture size by 23% in combination with improved growth conditions, and an even more significant reduction in dislocation density can be expected from further reducing the aperture size.

Using a sequential reformation/growth process to coalesce the layer, leads to high prevalence of current-leakage paths, associated with inversion domains. A prevalence of pinned dislocations was also observed in samples reformed by the sequential method. By instead using static reformation conditions in one continuous step, the formation of inversion domains was eliminated. Furthermore, dislocation-associated current-leakage paths, as observed by conductive AFM, were reduced to the coalesced interface, where both screw and mixed screw/edge type dislocations were found.

Having shown the large potential of GaN NW reformation for creating GaN substrates of superior quality, the viability of this method relies essentially on the potential to reduce the dislocations formed at the coalesced interface. The key task for going forward will be the systematic exploration of epitaxial conditions, such as pressure, temperature, or gas flows, enabled through the in-depth understanding of the origin and formation mechanisms of these dislocations that was obtained here.

ACKNOWLEDGMENTS

This work was performed within the NanoLund Centre for Nanoscience at Lund University, and was further supported by the Swedish Research Council (VR), the Swedish Foundation for Strategic Research (SSF), Grant No. 132141, the Vinnova innovation agency, Grant No. 2018 02149, the Knut and Alice Wallenberg Foundation, and the Swedish Energy Agency, Grant No 38344-1. The authors thank Hartmut Stadler from Bruker for experimental support and helpful discussions. The authors also thank Vanya Darakchieva and Rosalia Delgado Carrscon for providing XRD data for GaN/sapphire substrates.

---

[1] T. Fujii, Y. Gao, R. Sharma, E. L. Hu, S. P. DenBaars, and S. Nakamura, Increase in the extraction efficiency of GaN-based light-emitting diodes via surface roughening, Appl. Phys. Lett. **84**, 855 (2004).

[2] W. Utsumi, H. Saitoh, H. Kaneko, T. Watanuki, K. Aoki, and O. Shimomura, Congruent melting of gallium nitride at 6 GPa and its application to single-crystal growth, Nat. Mater. **2**, 735 (2003).

[3] S. Nakamura, InGaN-based violet laser diodes, Semicond. Sci. Technol. **14**, R27 (1999).

[4] D. W. Merfeld, X. A. Cao, S. F. Leboeuf, S. D. Arthur, J. W. Kretchmer, and M. P. D'evelyn, Influence of GaN material characteristics on device performance for blue and ultraviolet light-emitting diodes, J. Electron. Mater. **33**, 1401 (2004).

[5] T. Mukai, K. Takekawa, and S. Nakamura, InGaN-based blue light-emitting diodes grown on epitaxially laterally overgrown GaN substrates, Jpn. J. Appl. Phys. **37**, L839 (1998).

[6] A. P. Zhang, L. B. Rowland, E. B. Kaminsky, V. Tilak, J. C. Grande, J. Teetsov, A. Vertiatchikh, and L. F. Eastman, Correlation of device performance and defects in AlGaN/GaN high-electron mobility transistors, J. Electron. Mater. **32**, 388 (2003).

[7] B. S. Simpkins, D. M. Schaadt, E. T. Yu, and R. J. Molnar, Scanning Kelvin probe microscopy of surface electronic structure in GaN grown by hydride vapor phase epitaxy, J. Appl. Phys. **91**, 9924 (2002).

[8] S. L. Selvaraj, T. Suzue, and T. Egawa, Influence of deep pits on the breakdown of metalorganic chemical vapor deposition grown AlGaN/GaN high electron mobility transistors on silicon, Appl. Phys. Express **2**, 111005 (2009).

[9] T. S. Zheleva, O.-H. Nam, M. D. Bremser, and R. F. Davis, Dislocation density reduction via lateral epitaxy in selectively grown GaN structures, Appl. Phys. Lett. **71**, 2472 (1997).

[10] V. Bousquet, P. Vennéguès, B. Beaumont, M. Vaille, and P. Gibart, TEM study of the behavior of dislocations during ELO of GaN, Phys. Status Solidi (b) **216**, 691 (1999).

[11] B. Beaumont, V. Bousquet, P. Vennéguès, M. Vaille, A. Bouillé, P. Gibart, S. Dassonneville, A. Amokrane, and B. Sieber, A two-step method for epitaxial lateral overgrowth of GaN, Phys. Status Solidi (a) **176**, 567 (1999).

[12] P. Vennéguès, B. Beaumont, V. Bousquet, M. Vaille, and P. Gibart, Reduction mechanisms for defect densities in GaN using one- or two-step epitaxial lateral overgrowth methods, J. Appl. Phys. **87**, 4175 (2000).

[13] R. Colby, Z. Liang, I. H. Wildeson, D. A. Ewoldt, T. D. Sands, R. E. García, and E. A. Stach, Dislocation filtering in GaN nanostructures, Nano Lett. **10**, 1568 (2010).

[14] Y. Kato, S. Kitamura, K. Hiramatsu, and N. Sawaki, Selective growth of wurtzite GaN and $Al_xGa_{1-x}N$ on GaN/sapphire substrates by metalorganic vapor phase epitaxy, J. Cryst. Growth **144**, 133 (1994).

[15] T. Akasaka, Y. Kobayashi, S. Ando, and N. Kobayashi, GaN hexagonal microprisms with smooth vertical facets fabricated by selective metalorganic vapor phase epitaxy, Appl. Phys. Lett. **71**, 2196 (1997).

[16] B. Beaumont, P. Gibart, M. Vaille, S. Haffouz, G. Nataf, and A. Bouillé, Lateral overgrowth of GaN on patterned GaN/sapphire substrate via selective metal organic vapour phase epitaxy: A route to produce self supported GaN substrates, J. Cryst. Growth **189**, 97 (1998).

[17] T.-Y. Tang, W.-Y. Shiao, C.-H. Lin, K.-C. Shen, J.-J. Huang, S.-Y. Ting, T.-C. Liu, C. C. Yang, C.-L. Yao, J.-H. Yeh *et al.*, Coalescence overgrowth of GaN nanocolumns on sapphire with patterned metal organic vapor phase epitaxy, J. Appl. Phys. **105**, 023501 (2009).

[18] Y.-S. Chen, W.-Y. Shiao, T.-Y. Tang, W.-M. Chang, C.-H. Liao, C.-H. Lin, K.-C. Shen, C. C. Yang, M.-C. Hsu, J.-H. Yeh *et al.*, Threading dislocation evolution in patterned GaN nanocolumn growth and coalescence overgrowth, J. Appl. Phys. **106**, 023521 (2009).

[19] Z. Bi, F. Lenrick, J. Colvin, A. Gustafsson, O. Hultin, A. Nowzari, T. Lu, R. Wallenberg, R. Timm, A. Mikkelsen *et al.*, InGaN platelets: Synthesis and applications toward green and red light-emitting diodes, Nano Lett. **19**, 2832 (2019).

[20] S. J. Rosner, E. C. Carr, M. J. Ludowise, G. Girolami, and H. I. Erikson, Correlation of cathodoluminescence inhomogeneity with microstructural defects in epitaxial GaN grown by metalorganic chemical-vapor deposition, Appl. Phys. Lett. **70**, 420 (1997).

[21] P. J. Hansen, Y. E. Strausser, A. N. Erickson, E. J. Tarsa, P. Kozodoy, E. G. Brazel, J. P. Ibbetson, U. Mishra, V. Narayanamurti, S. P. DenBaars *et al.*, Scanning capacitance microscopy imaging of threading dislocations in GaN films grown on (0001) sapphire by metalorganic chemical vapor deposition, Appl. Phys. Lett. **72**, 2247 (1998).

[22] G. Koley and M. G. Spencer, Surface potential measurements on GaN and AlGaN/GaN heterostructures by scanning Kelvin probe microscopy, J. Appl. Phys. **90**, 337 (2001).

[23] B. S. Simpkins, E. T. Yu, P. Waltereit, and J. S. Speck, Correlated scanning Kelvin probe and conductive atomic force microscopy studies of dislocations in gallium nitride, J. Appl. Phys. **94**, 1448 (2003).

[24] D. Li, M. Sumiya, S. Fuke, D. Yang, D. Que, Y. Suzuki, and Y. Fukuda, Selective etching of GaN polar surface in potassium hydroxide solution studied by x-ray photoelectron spectroscopy, J. Appl. Phys. **90**, 4219 (2001).

[25] J. L. Rouviere, J. L. Weyher, M. Seelmann-Eggebert, and S. Porowski, Polarity determination for GaN films grown on (0001) sapphire and high-pressure-grown GaN single crystals, Appl. Phys. Lett. **73**, 668 (1998).

[26] J. L. Weyher, S. Müller, I. Grzegory, and S. Porowski, Chemical polishing of bulk and epitaxial GaN, J. Cryst. Growth **182**, 17 (1997).

[27] A. R. Smith, R. M. Feenstra, D. W. Greve, M.-S. Shin, M. Skowronski, J. Neugebauer, and J. E. Northrup, Determination of wurtzite GaN lattice polarity based on surface reconstruction, Appl. Phys. Lett. **72**, 2114 (1998).

[28] D. Zhuang and J. H. Edgar, Wet etching of GaN, AlN, and SiC: A review, Mater. Sci. Eng. R **48**, 1 (2005).

[29] E. S. Hellman, The polarity of GaN: A critical review, Mater. Res. Soc. Internet J. Nitride Semiconduct. Res. **3**, e11 (1998).

[30] J. Sumner, S. Das Bakshi, R. A. Oliver, M. J. Kappers, and C. J. Humphreys, Unintentional doping in GaN assessed by scanning capacitance microscopy, Phys. Status Solidi (b) **245**, 896 (2008).

[31] C. G. Van de Walle and J. Neugebauer, First-principles calculations for defects and impurities: Applications to III-nitrides, J. Appl. Phys. **95**, 3851 (2004).

[32] H. Xing, D. S. Green, H. Yu, T. Mates, P. Kozodoy, S. Keller, S. P. DenBaars, and U. K. Mishra, Memory effect and redistribution of Mg into sequentially regrown GaN layer by metalorganic chemical vapor deposition, Jpn. J. Appl. Phys. **42**, 50 (2003).

[33] D. Kapolnek, X. H. Wu, B. Heying, S. Keller, B. P. Keller, U. K. Mishra, S. P. DenBaars, and J. S. Speck, Structural evolution in epitaxial metalorganic chemical vapor deposition grown GaN films on sapphire, Appl. Phys. Lett. **67**, 1541 (1995).

[34] E. J. Tarsa, B. Heying, X. H. Wu, P. Fini, S. P. DenBaars, and J. S. Speck, Homoepitaxial growth of GaN under Ga-stable and N-stable conditions by plasma-assisted molecular beam epitaxy, J. Appl. Phys. **82**, 5472 (1997).

[35] J. W. P. Hsu, M. J. Manfra, S. N. G. Chu, C. H. Chen, L. N. Pfeiffer, and R. J. Molnar, Effect of growth stoichiometry on the electrical activity of screw dislocations in GaN films grown by molecular-beam epitaxy, Appl. Phys. Lett. **78**, 3980 (2001).

[36] J. E. Northrup, Screw dislocations in GaN: The Ga-filled core model, Appl. Phys. Lett. **78**, 2288 (2001).

[37] X. A. Cao, J. A. Teetsov, F. Shahedipour-Sandvik, and S. D. Arthur, Microstructural origin of leakage current in GaN/InGaN light-emitting diodes, J. Cryst. Growth **264**, 172 (2004).

[38] B. Heying, E. J. Tarsa, C. R. Elsass, P. Fini, S. P. DenBaars, and J. S. Speck, Dislocation mediated surface morphology of GaN, J. Appl. Phys. **85**, 6470 (1999).

[39] K. M. Jones, P. Visconti, F. Yun, A. A. Baski, and H. Morkoç, Investigation of inversion domains in GaN by electric-force microscopy, Appl. Phys. Lett. **78**, 2497 (2001).

[40] B. J. Rodriguez, W.-C. Yang, R. J. Nemanich, and A. Gruverman, Scanning probe investigation of surface charge and surface potential of GaN-based heterostructures, Appl. Phys. Lett. **86**, 112115 (2005).

[41] R. Katayama, Y. Kuge, K. Onabe, T. Matsushita, and T. Kondo, Complementary analyses on the local polarity in lateral polarity-inverted GaN heterostructure on sapphire (0001) substrate, Appl. Phys. Lett. **89**, 231910 (2006).

[42] J. Colvin, R. Ciechonski, A. Gustafsson, L. Samuelson, J. B. Ohlsson, R. Timm *et al.*, Local defect-enhanced anodic oxidation of reformed GaN nanowires (unpublished).

[43] G. P. Dimitrakopulos, A. M. Sanchez, Ph. Komninou, Th. Kehagias, Th. Karakostas, G. Nouet, and P. Ruterana, Interfacial steps, dislocations, and inversion domain boundaries in the GaN/AlN/Si (0001)/(111) epitaxial system, Phys. Status Solidi (b) **242**, 1617 (2005).

[44] A. M. Sanchez, G. Nouet, P. Ruterana, F. J. Pacheco, S. I. Molina, and R. Garcia, A mechanism for the multiple atomic configurations of inversion domain boundaries in GaN layers grown on Si (111), Appl. Phys. Lett. **79**, 3588 (2001).

[45] H. S. Kim, H. Lee, D. Jang, D. Kim, and C. Kim, Inversion domain boundary structure of laterally overgrown c-GaN domains including the inversion from Ga to N polarity at a mask pattern boundary, J. Appl. Crystallogr. **51**, 1551 (2018).

[46] J. Song, G. Yuan, K. Xiong, B. Leung, and J. Han, Epitaxial lateral overgrowth of nitrogen-polar (000-1) GaN by metalorganic chemical vapor deposition, Cryst. Growth Design **14**, 2510 (2014).

[47] C. Iwamoto, X.-Q. Shen, H. Okumura, H. Matsuhata, and Y. Ikuhara, Structure analysis of GaN thin film with inversion domains by high voltage atomic resolution microscopy, Mater. Trans. **43**, 1542 (2002).